Spatiospectral conditioning of laser-plasma-accelerated electron beams using electromagnetic solenoids

M. V. Ambat,[1,*] H. G. Rinderknecht,[1] J. Peebles,[1] D. Fess,[1] R. McEvoy,[1] C. D. Arrowsmith,[1] G. Bruhaug,[2] I. A. LaBelle,[1] M. A. VanDusen-Gross,[1] D. H. Froula,[1] and J. L. Shaw[1,†]

[1]*University of Rochester Laboratory for Laser Energetics, Rochester, New York 14623, USA*
[2]*Los Alamos National Laboratory, Los Alamos, New Mexico 87545, USA*

(Received 8 April 2026; accepted 28 September 2026; published 28 October 2026)

Microcoulomb-class electron beams from laser-plasma accelerators (LPAs) driven by kilojoule-class laser systems can enable high-flux electron radiography and copious secondary particle production. However, electron beam spatial properties such as transverse beam nonuniformity and large spatial scale at application sites can limit their utility. In this work, we demonstrate spatial conditioning of microcoulomb-class electron beams using electromagnetic solenoids as focusing optics. By applying ~10 T solenoidal fields, we focused the electron beam onto a detection plane and measured a fluence enhancement factor of 6 over unconditioned electron beams. The chromatic focusing of the solenoids improved the resolution of electron beam radiographs produced using the focused electron beam. We also demonstrate a method using angled electromagnetic solenoids to simultaneously condition LPA electron beam spatial and spectral properties. These features are attractive for applications because they enable the spatial separation of a narrow-energy-spread population of the electron beam from the bulk of the electron beam.

DOI: 10.1103/2dby-29s7

I. INTRODUCTION

Relativistic electron beams from laser-plasma accelerators (LPAs) are emerging as a more compact complement to traditional linear accelerators in the fields of femtosecond-scale probing [1,2], highly penetrative, micron-scale radiography of high-Z materials [3,4], and the production of secondary particles such as positrons [5–8], x-rays [9–26], and neutrons [27–30]. Recently, LPA platforms driven by kilojoule-class lasers have produced microcoulomb-class electron beams [31–33]. This exciting advancement can enable brighter electron radiography and the possibility of higher-yield conversion to secondary particles. The co-location of these platforms to multikilojoule high-energy-density-science (HEDS) drivers expands the usage of these LPA electron beams to a wider variety of experiments. However, these microcoulomb-class electron beams can suffer from inconsistent shot-to-shot pointing, severe nonuniformity in their spatial profiles, and a large spot size at application sites, which can limit their fluence and utility.

Magnetic lenses offer a solution to condition electron beams with large spot sizes and shot-to-shot pointing variability. Just as refraction in glass lenses bends and focuses light, the Lorentz force from a magnetic lens, $\vec{F} = d\vec{p}/dt = d(\gamma m_0 \vec{v})/dt = q\,(\vec{v} \times \vec{B})$, can bend electron trajectories and focus electron beams. Here, $\vec{p}$ is the electron momentum, γ is the relativistic Lorentz factor, m_0 is the electron rest mass, $\vec{v}$ is the electron velocity, $q = -e$ is the electron charge, and $\vec{B}$ is the magnetic field of the lens. Typically, magnetic quadrupole arrays [34–36] are used in radiofrequency linear accelerator facilities to focus and steer electron beams and have been demonstrated on LPAs [37]. However, such a focusing scheme requires multiple magnetic optics to condition the electron beam in two (transverse) spatial dimensions because a single quadrupole produces a focusing force in one transverse direction but a defocusing force in the other transverse direction. Additionally, these devices can often have a large footprint consisting of bulky permanent magnet polepieces and additional infrastructure [38], which can make them challenging to implement on HEDS drivers.

A simpler, rapidly tunable, single-element, magnetic focusing scheme that exploits cylindrical symmetry is a solenoid. Electrons propagating through solenoidal magnetic fields exhibit simple harmonic motion about the

*Contact author: mvambat@lanl.gov
†Contact author: jshaw05@lle.rochester.edu

Published by the American Physical Society under the terms of the Creative Commons Attribution 4.0 International license. Further distribution of this work must maintain attribution to the author(s) and the published article's title, journal citation, and DOI.

solenoid axis. The periodicity of this motion can be intentionally tailored for a certain electron energy by selecting a specific solenoid field strength to enable point-to-point imaging from an electron source at the object plane to a detector at an image plane. The thin-lens focal length f of a single-turn, current-carrying solenoid is given by Busch's theorem [39,40],

$$\frac{1}{f} = \kappa^2 \int B_z^2 dz, \tag{1}$$

where $\kappa^2 \equiv e^2c^2/4(E_k^2 + 2E_kE_0)$, E_k is the electron kinetic energy, $E_0 = m_0c^2$ is the electron rest energy, and B_z is the longitudinal magnetic field of the solenoid. In the thin-lens approximation, electrons with an energy that satisfies the relation $1/f = 1/z_0 + 1/z_i$, where z_0 and z_i are the object and image distances, respectively, come to focus at the detection plane.

In this paper, we present spatiospectral conditioning of microcoulomb-class LPA-produced electron beams using electromagnetic solenoids. In Sec. II, we lay out a generalized experimental platform that enabled solenoidal electron beam conditioning. In Sec. III, we show electron beam focusing at the detector plane and an electron beam fluence enhancement factor of 6 over unconditioned electron beams. We investigate the effects of solenoid astigmatism on the observables. Using the conditioned electron beams yielded up to a factor of 3 improvement in electron radiography resolution over unconditioned electron beams. In Sec. IV, we describe the physical picture of spatiospectral electron beam conditioning using electromagnetic solenoids at an angle with respect to the optical axis. A modified experimental setup allowed for the interrogation of spatiospectral conditioning for the first time. We conclude with remarks on applying this technique for future studies.

II. GENERAL EXPERIMENTAL SETUP

Experiments were performed on the OMEGA EP laser system at the Laboratory for Laser Energetics [41]. The laser was operated with a central wavelength of $\lambda_0 = 1054$ nm and a pulse duration of 700 ± 100 fs. To increase the Rayleigh range, spatially filtered apodizers [42] converted the nominal $f/2$ focal geometry to an $f/5$ geometry. The average $1/e^2$ focal spot size (radius) of the laser was 8 ± 1 μm. The on-target laser energy ranged from 31 to 96 J, producing on-target peak normalized laser vector potentials ($a_0 \cong 8.6 \times 10^{-10} \sqrt{I_0[\mathrm{W/cm^2}]}\,\lambda_0[\mu\mathrm{m}]$, where I_0 is the vacuum laser intensity) between 5.9 and 10.8 ± 0.2. The laser was focused 500 μm inside a Mach 5 gas jet with a 6 mm nozzle diameter as shown in Fig. 1. The optical axis was 1.8 mm above the gas jet nozzle. Pure helium was used on all shots, and the average plateau plasma density across the central 4 mm according to [43] was 4.1×10^{18} cm^{-3}.

Downstream of the gas jet in the $+z$ direction, an electromagnetic solenoid intercepted the electron beam. The solenoids consisted of four turns of 18 AWG copper wire. The solenoids were pulsed by the Magneto-Inertial Fusion Electrical Discharge System (MIFEDS) [44,45] with voltages in the range of 10–15 kV, resulting in currents of 24–36 kA and nominal magnetic flux densities at the solenoid centers B_0 of 7–12 T. The MIFEDS pulse had a rise time of ~1 μs and a flattop window (the time interval where the current, and therefore the magnetic field, is constant to within ±5%) of ~700 ns. According to Eq. (1), electrons of a specific energy E_f were focused at a detection plane some distance L_{det} away. Electrons with energies above E_f possessed a focal length greater than L_{det} and were less focused. Put another way, higher-energy electrons experienced a weaker focusing force and therefore subtended a larger solid angle than the focused

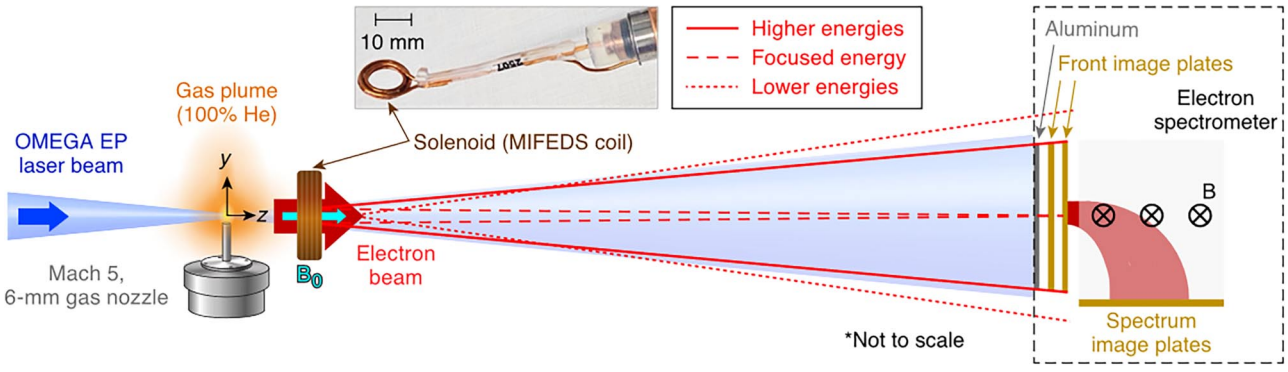


FIG 1. Experimental layout. The laser beam (blue) was focused onto a supersonic gas plume (orange). The electron beam (red) was intercepted by a solenoid (brown) with the solenoid axis (teal arrow) nominally pointing in the $+z$ direction, parallel to the optical axis. A photo of an as-deployed solenoid is included for reference. Given the solenoid field strength and distance between the gas jet nozzle exit and detection plane, the solenoid preferentially focused electrons of a certain energy (red dashed lines). Typical trajectory envelopes of higher- and lower-energy electrons are plotted in solid and dotted lines, respectively. The resulting spatial and spectral conditioning due to the solenoid was observed on image plates (yellow) in a downstream electron spectrometer (dashed black box).

energies at the detection plane. Electrons with energies below E_f came to a focus before L_{det} and tended to diverge at the detection plane. Due to this energy dependence, variability in the native electron beam spectrum can impact the electron beam spot size at the detection plane on each shot.

The accelerated electrons co-propagated with the laser toward an electron spectrometer that measured two key electron beam observables: spatial profile and spectrum. The front of the electron spectrometer held 50-μm-thick aluminum foil to block laser light in front of image plates (IPs) that intercepted the electron beams. These "front" IPs provided information on the transverse electron beam spatial profile, pointing, and total charge. Electrons that passed through the electron spectrometer aperture propagated through a gap formed by two permanent magnets. The trajectories of these electrons were bent by this dipolar magnetic field, and the electrons were recorded by a "spectrum" IP. The details of the solenoids and the electron spectrometers in each of our two experimental setups are discussed in Secs. III B and IV B.

III. FOCUSING RELATIVISTIC ELECTRON BEAMS USING MIFEDS SOLENOIDS

A. Initial Boris pusher predictions

Simulations using a Boris pusher algorithm [46] guided the experimental design and offered predictions of the electron beam experimental observables. For details on our Boris pusher simulations, which neglect space charge, see Appendix A. The spatial profile of the input electron beam was taken from a measured spatial profile without solenoidal conditioning with an artificial, circular, fourth-order super-Gaussian mask applied, as shown in Fig. 2(a). The input electron beam spectrum [Fig. 2(d)] was taken from the measured electron beam spectrum of the same shot. The simulations assumed an input electron beam source size radius w_0 of 16 μm and a full-angle electron beam divergence of 160 mrad. The simulated solenoid consisted of two inner windings with radius $R = 5.65$ mm and two outer windings with $R = 6.95$ mm. The solenoid was placed 6.6 mm away from the electron source (object distance) and 464.2 mm away from the detection plane (image distance). These simulation parameters match the experimental details described in the next section.

Simulations predict that the electron beam can be focused to a round, 0.5-mm (FWHM) spot size at the detection plane after the electron beam propagates through solenoids with the nominal range of B_0 produced in the experiment for electron energies between 6.1 and 11.0 MeV [Figs. 2(b) and 2(c)]. The color bars of these conditioned output spatial profiles have higher maxima than the unconditioned spatial profile owing to the electron beam fluence enhancement near the electron beam focus at the detection plane center. Electrons that land within a 1-mm-diameter circle centered at the detection plane (representing the real electron spectrometer aperture) contribute to the predicted electron spectra shown in Figs. 2(e) and 2(f). Electrons of the focused energy E_f are focused into the spectrometer aperture. This results in a prominent, narrow peak, delineated in dashed red, on top of the nominal electron spectrum due to the highly chromatic focusing of the solenoid as observed in previous experiments [37,47].

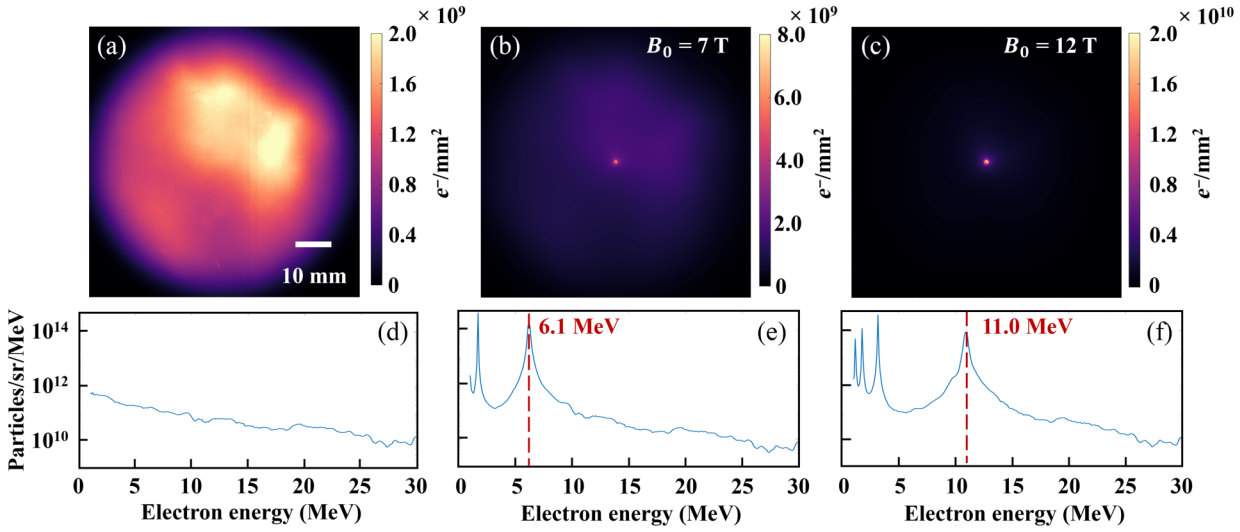


FIG 2. Boris pusher simulation predictions of the experimental observables. (a) Electron beam spatial profile without solenoidal conditioning. (b), (c) Electron beam spatial profiles with solenoidal conditioning for $B_0 = 7$ and 12 T, respectively. In (a)–(c), electrons propagate into the page. (d) Electron spectrum without solenoidal conditioning. (e), (f) Electron spectra with solenoidal conditioning for B_0 of 7 and 12 T, respectively. Red dashed lines indicate the primary focused energy. Additional peaks appear for lower energies that satisfy Eq. (3).

Additional peaks appear at lower electron energies in Figs. 2(e) and 2(f). These peaks correspond to foci formed by electrons of particular lower energies that oscillate for more than one period in the solenoid field and were refocused at the detection plane. To explain this, we briefly describe the energy-dependent focal length of a solenoid, with the full treatment given in Appendix B. Dropping the thin-lens approximation and assuming a longitudinal solenoid magnetic field of the form (Glaser's bell-shaped field [40,48]):

$$B(z) = \frac{B_0}{1 + (z/a)^2}, \tag{2}$$

where B_0 is the magnetic field at the solenoid center and a is the full width at half maximum of $B(z)$ (in practice, this is approximately the solenoid radius, R), the focal length of the solenoid is

$$f = a \csc(n\pi/\omega), \tag{3}$$

where $n = 1, 2, \ldots$, $\omega = \sqrt{1 + k^2}$ is an energy-dependent lens strength parameter, and $k^2 = e^2c^2B_0^2a^2/4(E_k^2 + 2E_kE_0)$. The focused energy E_f is calculated for $n = 1$, which is given by

$$E_f = E_0\left[\frac{1}{2}\sqrt{1 + \frac{e^2c^2B_0^2a^2}{E_0^2K^2(n)}} - 1\right], \tag{4}$$

where

$$K^2(n) \equiv \Omega^2(n) - 1 \tag{5}$$

and

$$\Omega(n) \equiv \frac{n\pi}{\pi - \cot^{-1}\left(\frac{a^2 + z_0z_i}{az_0 - az_i}\right)}. \tag{6}$$

From Eq. (3), multiple foci can occur once $\omega \geq 2$, which is approximately satisfied when $E_k < ecB_0a/2\sqrt{3} \equiv E_{mf}$, which is equivalent to

$$E_{mf}\,[\mathrm{MeV}] = 0.0866\ B_0[T]\,R[\mathrm{mm}]. \tag{7}$$

Electrons with energies below E_{mf} can form multiple foci between the solenoid and the detection plane, and electrons with energies that satisfy Eqs. (3)–(6) for integers $n > 2$ will form a focus at the detection plane. For the solenoid field strengths in this experiment, $E_{mf} \approx 3$–5 MeV. We find excellent agreement between the focused energies for $B_0 = 7$ and 12 T predicted by the analytical theory ($E_f = 6.2$ and 10.9 MeV, respectively) and by the Boris pusher simulations ($E_f = 6.1$ and 11.0 MeV, respectively).

B. Experimental setup—solenoids and Electron-Positron-Proton Spectrometer

To investigate solenoidal focusing of the LPA-produced electron beams, we used solenoids with four windings arranged as two inner windings with radius $R = 5.65$ mm and two outer windings with $R = 6.95$ mm. The solenoids were centered on the laser axis 6.6 mm downstream from the gas jet nozzle exit.

The Electron-Positron-Proton Spectrometer (EPPS) [49] was used to record electron beam spatial profiles and spectra. The front of the EPPS was placed 476.3 mm away from the laser focus (464.2 mm away from the solenoids). The dimensions of the EPPS front IPs were 76.2 mm × 76.2 mm. The front IP stack held two IPs. The first IP (the one closest to the LPA) filtered out electrons with kinetic energies below 0.4 MeV and was generally used for rapid, qualitative assessment of the electron beam spatial profile after each shot. The second IP recorded the electron beam spatial profiles reported in this manuscript. On some shots, contact radiography test objects and a third IP were added behind the second IP in the front IP stack. These front IPs were scanned with a resolution of 50 μm. The EPPS shielding fully encloses the diagnostic to reduce noise. The front shielding of the EPPS dipole magnets consisted of 1.27 cm of Al-6061, 5.08 cm of a 94%-lead and 6%-antimony alloy, and 1.27 cm of 1008 steel, and the spectrometer aperture was 1-mm in diameter. Fujifilm BAS-MS IPs were used for all EPPS front IPs and spectrum IPs.

C. Experimental results—electron beam focusing

The conditioned electron beams observed using solenoidal focusing represent a significant improvement in the spatial profile quality and fluence while maintaining high charge throughput as seen by comparing Figs. 3(a)–3(c) to Fig. 3(d). Unconditioned electron beams produced on the OMEGA EP LPA platform possess total charge ranging from 300 to 700 nC using identical laser-plasma parameters [31] as the present study, and we observe comparable total charge on the front IPs in the conditioned electron beams as summarized in Table I. The FWHM electron beam spot size at the detector was steadily reduced to a minimum value of 18 mm as the solenoid field strength, and thus the solenoid focusing power, was increased [Fig. 3(e)]. This led to an electron beam fluence enhancement factor of 6 at the detector plane, where the maximum electron fluence in shot B ($\sim 2.4 \times 10^9$ electrons/mm^2, with solenoid) is 6 times greater than that in shot 0 ($\sim 0.4 \times 10^9$ electrons/mm^2, without solenoid). We also observed that the electron beam centroid was not at the center of the detector plane on every shot, and we attribute this to pointing variations in the native electron beam by up to 45 mrad with respect to the optical axis [50]. The electron beam spatial profiles that employed solenoidal

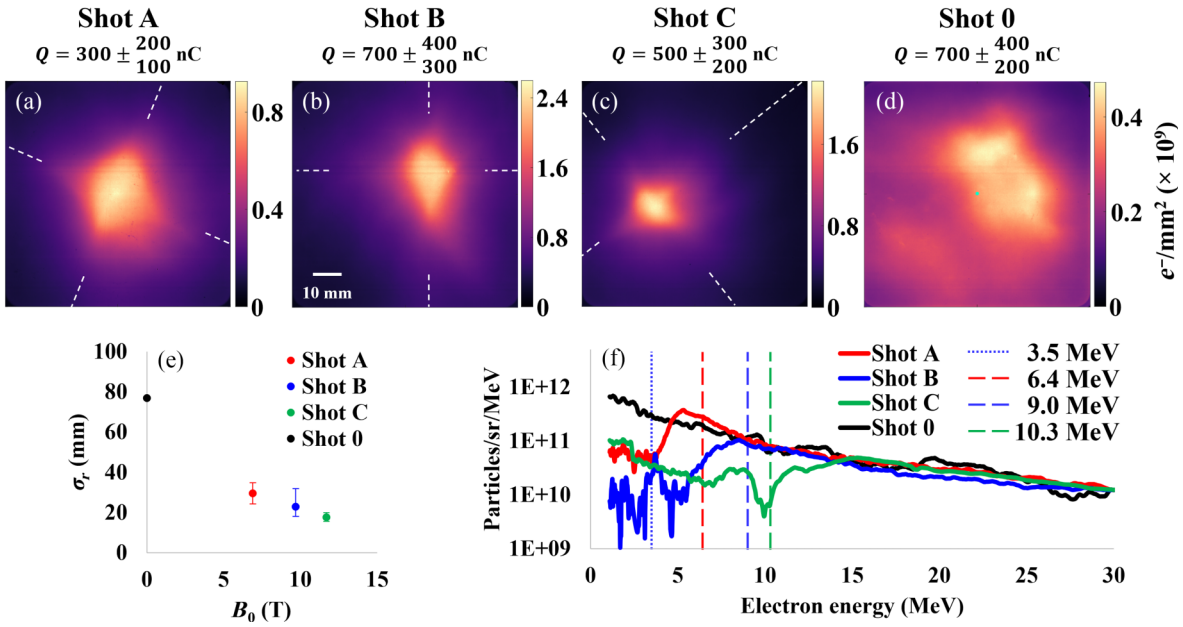


FIG 3. Measurements of electron beam spatial profiles and spectra. (a)–(c) Electron beam spatial profiles from the EPPS front IP with solenoidal conditioning for $B_0 = 6.9, 9.7$, and 11.7 T, respectively. (d) Electron beam spatial profile from the EPPS front IP without solenoidal conditioning. For (a)–(d), electrons propagate into the page. The total charge incident on the front IPs, Q, is calculated following the methodology in Ref [31]. (e) Azimuthally averaged FWHMs of the electron beam spot size from (a)–(d). The error bars span the minimum and maximum values for the FWHMs of each spatial profile. Note that σ_r cannot be adequately assessed for shot 0 because the electron beam overfills the IP and exhibits severe nonuniformity, so the front IP width is listed for comparison. Superimposed on (d) is a teal circle denoting the EPPS aperture. Electrons propagating through the aperture contribute to (f) electron spectra corresponding to the four shots in (a)–(d). The vertical dashed lines indicate the focused electron energy E_f predicted by Boris pusher simulations. The raw spectra of shots A, B, and C were each multiplied by a factor of 1.7, 0.6, and 0.3, respectively, to produce the curves shown in this figure; in this manner, all four spectra have the same value at 30 MeV for visual clarity.

focusing exhibited a diamondlike shape. Dashed white lines are drawn at the edges of the spatial profiles of shots A, B, and C to indicate the diagonals, and these features are further investigated and discussed in the next section.

Because electrons at the focused energies possess a smaller spot size and are most sensitive to the electron beam pointing, solenoidal focusing acts as a highly chromatic energy filter as shown in the electron spectra in Fig. 3(f). For shot A [Fig. 3(a)], Boris pusher simulations predict peaks in the corresponding electron spectrum at 1.7 and 6.4 MeV. We observe an order of magnitude fewer electrons below 5.8 MeV, which is reasonably close to the predicted focused energy of 6.4 MeV. We do not observe a clear second peak in the spectrum at 1.7 MeV: we hypothesize that this is because there is a substantial bremsstrahlung background in the spectrum IPs below 4 MeV, and the predicted peak at 1.7 MeV may have been lost in the background subtraction. The amount of charge at the focused energy can be calculated using the measured spectrum only when the

TABLE I. Summary of experimental inputs and electron beam front IP observables presented in Fig. 3. E_{laser}: laser energy on-target, a_0: normalized laser vector potential, B_0: magnetic flux density at the solenoid center, $\sigma_x \times \sigma_y$: FWHM of the major and minor axes of the electron beam spatial profile, σ_r: azimuthally averaged FWHM of the electron beam spatial profile, Q_{tot}: total charge incident on the front IP.

	Experimental inputs			Electron beam front IP observables		
Shot	E_{laser} (J)	a_0	B_0 (T)	$\sigma_x \times \sigma_y$(mm × mm)	σ_r (mm)	Q_{tot} (nC)
A	45.8	8.4	6.9	35 × 33	29	$300 \pm {}^{200}_{100}$
B	91.4	9.9	9.7	32 × 24	24	$700 \pm {}^{400}_{300}$
C	55.0	6.8	11.7	18 × 18	18	$500 \pm {}^{300}_{200}$
0	110.2	12.8	No solenoid	>76 × >76	⋯	$700 \pm {}^{400}_{200}$

electron beam is well-centered on the detector; for shot A, we measured ∼1 nC of charge at 5.8 MeV. In shot B, we observe prominences at 3.7 and 8.3 MeV, energies very close to those predicted by Boris pusher simulations (3.5 MeV, dotted blue line, and 9.0 MeV, dashed blue line). The electron spectrum of shot C shows a depression at 10.0 MeV, suggesting that electrons of this energy were strongly focused but missed the electron spectrometer aperture, which is consistent with the peak being 15 mm from the center of the detector as seen in Fig. 3(c). The energy of this sharp null feature is in excellent agreement with the predicted energy from both analytical theory [10.6 MeV, Eqs. (4)–(6)] and Boris pusher simulations (10.3 MeV, dashed green line).

D. Effects of solenoid astigmatism and electron beam spectrum on electron beam spatial profiles

Refined Boris pusher simulations [Figs. 4(a) and 4(b)] show that astigmatism in the solenoid is the main cause for the increased electron beam spatial profile size and diamondlike shape observed in the experiments when compared to initial simulation predictions (cf. Fig. 2). The astigmatism is due to the solenoid windings being elliptical as opposed to perfectly circular, which can be caused by manufacturing imperfections or the expansion of the solenoid as it is pulsed with current. Like most lens

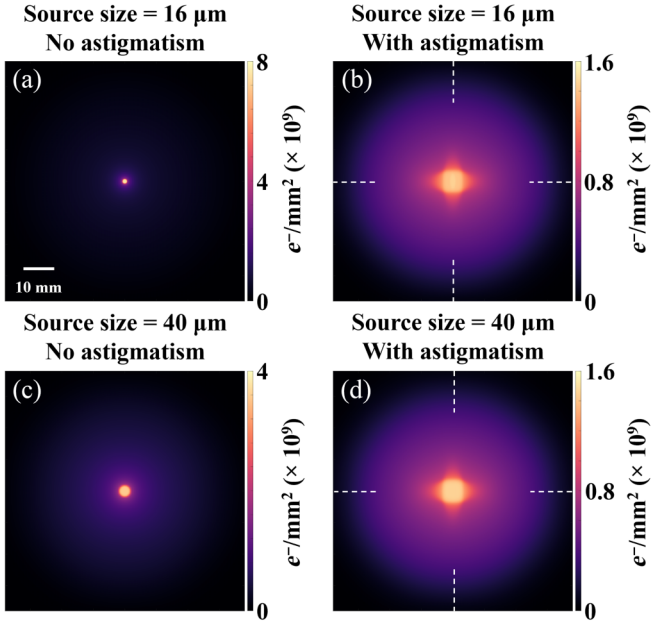


FIG 4. Boris pusher simulations demonstrating the effects of solenoidal astigmatism and electron source size on the resulting electron beam spatial profiles. (a) Nominal electron beam source size without astigmatism in the solenoid. (b) Nominal electron beam source size with astigmatism in the solenoid. (c) Larger electron beam source size without astigmatism in the solenoid. (d) Larger electron beam source size with astigmatism in the solenoid.

aberrations, astigmatism increases the electron beam image size at the detection plane, and early electron microscope experiments [51,52] have linked this diamond-like shape directly to astigmatism. Two sources of the variation in the angular orientation of the diamondlike profiles include variation in the coil-to-coil winding and the inherent image rotation, commonly studied in electron microscopy [40,52,53], which depends on both magnetic field strength and electron energy. To investigate the effects of astigmatism on electron beam spatial profiles, we simulated a single-turn elliptical solenoid ($B_0 = 11.7$ T) with major and minor axes of 7.6 and 6.3 mm, respectively. The solenoid minor axis was taken as the average radius of the inner windings (5.65 mm) and the outer windings (6.95 mm) of the actual solenoid used in the experiment. The input spatial profile to the new simulations was a spatially smoothed version of Fig. 2(a). The solenoid was placed 6.6 mm away from the electron source (object distance) and 464.2 mm away from the detection plane (image distance). By including astigmatism, the electron beam spot size at the detector grew from a radially symmetric Gaussian with a FWHM = 0.5 mm [Fig. 4(a)] to a diamond with an azimuthally averaged FWHM = 27.5 mm [Fig. 4(b)]. The astigmatism plays a much larger role than an increased electron source size as seen in Figs. 4(c) and 4(d). An electron beam source size larger than the laser spot has been observed in some simulations for LPAs operating in a similar regime [11] due to enhanced electron transverse oscillations within the LPA as a result of direct laser acceleration.

Even if solenoid astigmatism is present, the size of the electron beam spatial profiles also depends heavily on the electron beam spectrum, as shown in Figs. 5(a)–5(f). These simulations used the same solenoid geometry and object and image distances as those described in the previous paragraph, and the electron source size was 16 μm. Using the same field strengths as shots A, B, and C but with two different unconditioned spectra [Fig. 5(g)], we find that the electron beam spot size at the detector plane can span a wide range from ∼8 to ∼55 mm FWHM [Fig. 5(h)]. Because spectrum 1 [magenta, Fig. 5(g)] has more electrons above ∼11 MeV than spectrum 2 [cyan, Fig. 5(g)], the solenoid field strengths (6.9–11.7 T) are not high enough to focus the bulk of the electron beam. Therefore, the electron beam spatial profiles in Figs. 5(a)–5(c) are larger than those in Figs. 5(d)–5(f).

E. Experimental results—electron radiography resolution improvement

Since electron radiography resolution improves as the electron beam energy spread decreases [54], solenoidal focusing is predicted to improve electron radiography resolution. To investigate this, we radiographed static test objects consisting of discrete steps with thickness varying from 0.56 to 3.35 mm in 0.56 mm increments and with

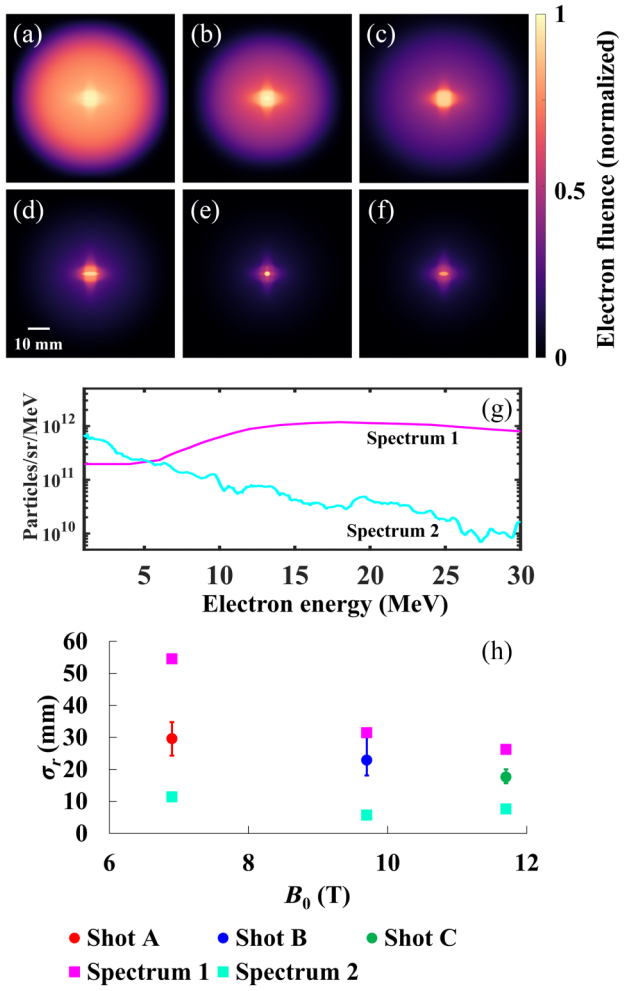


FIG 5. Boris pusher simulations demonstrating the effects of spectrum on the resulting electron beam spatial profiles with solenoid astigmatism included. (a)–(c) Electron beam spatial profiles for $B_0 = 6.9, 9.7$, and 11.7 T, respectively, using spectrum 1 [magenta in (g)]. (d)–(f) Electron beam spatial profiles for $B_0 = 6.9, 9.7$, and 11.7 T, respectively, using spectrum 2 [cyan in (g)]. (g) Two unconditioned electron spectra from two separate shots. (h) Azimuthally averaged FWHMs of the electron beam spot size from (a)–(f). The error bar lies within the marker size. The data from the experiment from Fig. 4(e) are included for comparison.

holes of diameters varying from 0.254 to 1.270 mm in 0.254 mm increments drilled throughout the steps. For a full description of the radiography test objects and method used to analyze the flattened radiographs shown in Figs. 6(a) and 6(b), see [3].

The radiography resolution achieved using the conditioned electron beam is up to a factor of 3 better than that achieved using the unconditioned electron beam. Transitions at edges (from step to step and across each hole) appear sharper in the radiograph with solenoidal conditioning [Fig. 6(b)] than in the radiograph without solenoidal conditioning [Fig. 6(a)], and we see this

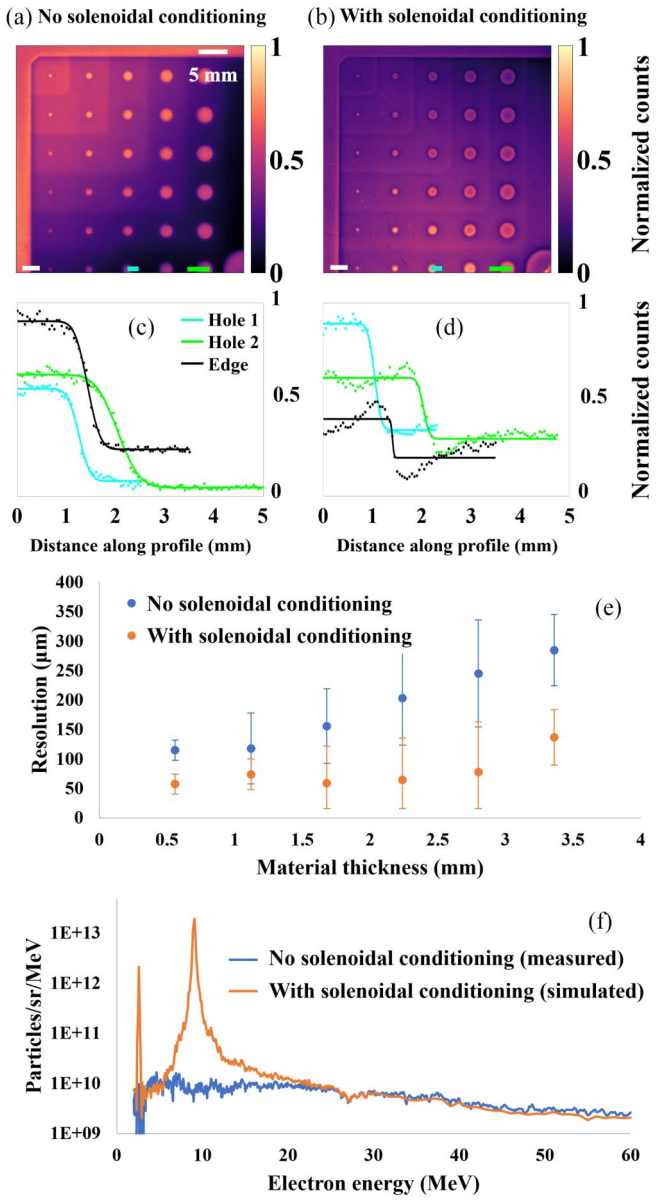


FIG 6. Contact electron radiography using electron beams with and without solenoidal conditioning. (a), (b) Flattened electron radiographs of a tin test object without and with, respectively, solenoidal conditioning. Material thickness increases from the top left corner to the bottom right corner in each image. This tin contact radiography object is in one quadrant of the front of the EPPS, and the spectrometer aperture (i.e., the detector center) is located at the top left corner in both images. Superimposed toward the bottom of the radiographs are lines indicating (c), (d) example lineouts and error function fits to sharp edges in the radiographs without and with, respectively, solenoidal conditioning. The material thickness for all these features is 4.00 mm. (e) Electron radiography resolution as a function of material thickness without (blue) and with (orange) solenoidal conditioning. (f) Electron beam spectrum without (blue, measured) and with (orange, simulated) solenoidal conditioning. The solenoid field strength was $B_0 = 10.0$ T, and simulations predict focused energies of 9.0 and 2.5 MeV.

quantitatively in representative lineouts used in the analysis [Figs. 6(c) and 6(d)]. These lineouts are error function fits to the data of the form $y = a + b\,\mathrm{erf}(\frac{x-c}{d})$, where d is the radiography resolution reported in Fig. 6(e). The ratio of the radiography resolution without solenoidal conditioning to the radiography resolution with solenoidal conditioning exhibits a maximum value of 3.14 for a material thickness of 2.8 mm. The improvement to the radiography resolution is due to the increase of electrons of the focused energy on the radiography object and the corresponding relative decrease in the electron energy spread, as shown in Fig. 6(f). The chromaticity of solenoidal focusing also results in more pronounced limb brightening [55], which occurs when electrons scatter off sharp edges, resulting in a dark doughnut shape around each hole as opposed to a smoother transition from the metal rim to the empty space. Similar to Snell's law of refraction in light optics, the angle at which the electron scatters depends on the electron's kinetic energy. This chromatic phenomenon manifests less severely for a broader electron beam spectrum because the overlapping scattering from the various energies will tend to blur out the overall effect. Thus, the limb brightening is more noticeable in the radiograph using the conditioned electron beam [Fig. 6(b)] than the unconditioned electron beam [Fig. 6(a)], and it is accompanied by a considerable improvement in the achievable resolution [Fig. 6(e)].

IV. SPATIOSPECTRAL CONDITIONING OF RELATIVISTIC ELECTRON BEAMS

A. Physical picture

Angled solenoids enable simultaneous focusing of a narrow-energy-spread population of the electron beam and the spatial separation of this population from the bulk of the electron beam. This "spatiospectral" conditioning can be mapped onto a detection plane using Boris pusher simulations as shown in Fig. 7 for various experimental parameters. A typical electron beam spatial profile conditioned by this capability is shown in Fig. 7(a), where the electron focus feature (highest fluence) is located at $(x, y)[\mathrm{mm}] = (66, -50)$, swept down and to the right of the bulk electron beam. The predominant focused energy is $E_f = 11.2$ MeV, and the focus feature in Fig. 7(a) has a FWHM energy spread of 1 MeV. The curves in Figs. 7(b)–7(d) show the mapping of individual electron energies at the detection plane for different solenoid field strengths B_0, solenoid angles θ_x and θ_y, and detection plane distances from the origin L_{det}. Single electrons were initialized at the origin, $(x, y, z) = (0, 0, 0)$ (see Fig. 1), with their velocities parallel to the $+z$ axis. Positive values of θ_x represent a solenoid angle tilted away from the $+z$ axis toward the $+x$ axis, and positive values of θ_y represent a solenoid angle tilted toward the $+y$ axis, where the $+z$ axis is directed out of the page in Fig. 7. The curves

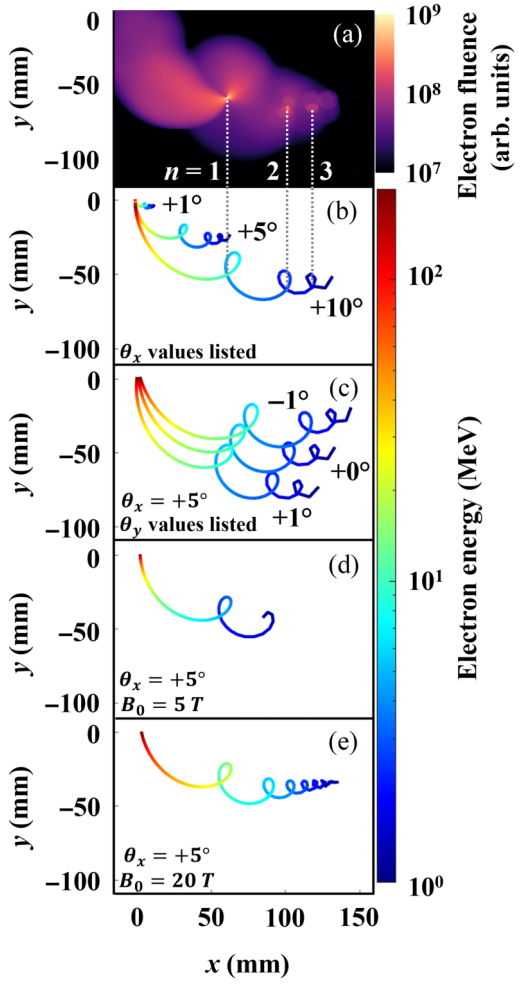


FIG 7. Boris pusher calculations of spatiospectral conditioning. Electrons propagate out of the page. (a) Electron beam spatial profile. $B_0 = 9.1$ T, $\theta_x = +10°$, $\theta_y = 0°$, $L_{\mathrm{det}} = 343$ mm. The input electron beam profile and spectrum are shown in Figs. 2(a) and 2(b). The electron source size is 16 μm and there is no astigmatism in the solenoid. Integer values of n that satisfy Eqs. (3)–(6), corresponding to each focus, are denoted in white. (b) Electron location as a function of electron energy for $\theta_x = +1°, +5°$, and $+10°$. Here, $B_0 = 9.1$ T, $\theta_y = 0°$, and $L_{\mathrm{det}} = 343$ mm. The curve for $\theta_x = +10°$ corresponds to the spatial profile shown in (a). (c) Electron location as a function of electron energy for $\theta_y = -1°, 0°$, and $+1°$. Here, $B_0 = 9.1$ T, $\theta_x = +5°$, and $L_{\mathrm{det}} = 700$ mm. L_{det} was changed from 343 mm in (b) to 700 mm in (c) to improve visualization by increasing the separation of the three curves. (d), (e) Electron location as a function of electron energy for $B_0 = 5$ and 20 T, respectively. Here, $\theta_x = +5°$, $\theta_y = 0°$, and $L_{\mathrm{det}} = 700$ mm.

exhibit loops, and each intersection corresponds to an electron energy that is focused at the detection plane according to Eqs. (3)–(6). The correspondence between each intersection with a focus is indicated by the vertical dotted lines that project the intersections in Fig. 7(b) onto the foci in Fig. 7(a), where Fig. 7(a) was modeled with the same parameters as the curve in Fig. 7(b) for $\theta_x = +10°$.

The Boris pusher calculations in Fig. 7 demonstrate key effects of input variables on the resulting observables. Increasing the solenoid angle θ_x from $+1°$ to $+10°$ results in the electrons intersecting the detection plane further from $(x, y) = (0, 0)$, as shown in Fig. 7(b). This informs the necessary solenoid angle magnitude for sufficiently separating the electron energies of interest from the bulk when the detection plane distance is fixed. Varying θ_y in 1° steps for a fixed θ_x reveals the relative angular tolerance required to achieve the desired focusing and steering [Fig. 7(c)]. The result of varying only the solenoid field strength is captured in Figs. 7(d) and 7(e), where $B_0 = 5$ and 20 T, respectively. The path traced by the electrons at the detection plane is identical in both Figs. 7(d) and 7(e) for $x < 90$ mm, but the location where the electron energies lie along the path is determined by the solenoid field strength. Furthermore, as shown in Fig. 7(e), the path traced by the electrons is extended beyond $x > 90$ mm and additional loops are produced as a direct result of B_0 increasing. The key takeaway from Figs. 7(d) and 7(e) is that for a fixed solenoid angle and detection plane distance, one can tune the focused electron energy E_f by simply tuning the solenoid field strength (in practice, via the solenoid pulser voltage or current). The x–y location of the electron focus feature remains in the same location (i.e., at the intersection of the loop nearest $(x, y) = (0, 0)$), and this can be advantageous to experiments that not only want to separate a narrow-energy-spread portion of the electron beam from the bulk but also tune the central electron energy at that focus.

B. Experimental setup—solenoids and Osaka University Electron Spectrometer

To explore spatiospectral conditioning of the LPA-produced electron beams, we used solenoids with four windings arranged in a single row with inner radius $R = 6.65$ mm. The centroid of the solenoid winding closest to the gas jet nozzle was placed at $(x, y, z)[\text{mm}] = (1.0, -0.6, 5.9)$ (here, the origin is at the gas jet exit along the optical axis) with the solenoid angle $(\theta_x, \theta_y) = (+5°, 0°)$. This location and angle of the solenoid produced an electron beam focus $+10°$ off the optical axis. Solenoid field strengths $B_0 \sim 10$ T are predicted to focus electrons with energies $E_f \sim 10$ MeV.

The Osaka University electron spectrometer (OU-ESM) [56], which consists of 5 spectrometer channels angled at $-10°, -5°, 0°, +5°$, and $+10°$ with respect to the optical axis, offered the capability to measure spatial profiles and spectra of electron beams steered by the angled solenoids. The front of the OU-ESM was placed 343.0 mm away from the laser focus (329.7 mm away from the solenoids). The dimensions of the OU-ESM front IPs were 140 mm × 20 mm. The front IP stack held two IPs. The first IP (the one closest to the LPA) filtered out electrons with kinetic energies below 0.3 MeV and was generally used for rapid, qualitative assessment of the electron beam spatial profile after each shot. The second IP recorded the electron beam spatial profiles, which are reported in this manuscript. These front IPs were scanned with a resolution of 50 μm. The OU-ESM shielding fully encloses the diagnostic to reduce noise. The front shielding of the OU-ESM dipole magnets consisted of 2.00 cm of tungsten, and the spectrometer aperture was 3 mm in diameter. Fujifilm BAS-SR IPs were used for all OU-ESM front IPs and spectrum IPs.

C. Simulation predictions and experimental results

Spatial profile and spectrum measurements of spatiospectrally conditioned electron beams validate the use of angled solenoids to steer focused energies to a desired location at a detection plane. We found that in order to reproduce the experimental results, the Boris pusher simulations needed to account for three additional factors: deviations in the solenoid angle within its range of positioning uncertainty ($\pm 1°$ in both θ_x and θ_y), electron beam pointing, and more severe astigmatism. We found that the electron focus feature predicted by initial Boris pusher simulations in Fig. 8(a) was broadened when astigmatism was included in the solenoids and when the electron source size was increased from 16 to 40 μm, as shown in Fig. 8(b), which is consistent with our findings in Sec. III C. However, angled solenoids are also particularly sensitive to electron beam pointing in contrast to on-axis, 0° solenoids (cf. Sec. III), which exploit cylindrical symmetry to focus electron beams. We performed 20 simulations scanning the uncertainty of solenoid angle, astigmatism, and electron beam pointing with respect to the optical axis, which is known to be up to 45 mrad for unconditioned electron beams. The electron beam spatial profile from our simulations [Fig. 8(c)] that best matched the electron beam spatial profiles from our experimental data [Figs. 8(d) and 8(e)] used a solenoid angle $(\theta_x, \theta_y) = (+6°, +1°)$, solenoid major and minor axes of 6.95 and 9.95 mm, respectively, and an electron beam pointing of 45 mrad off the optical axis (at an angle of $+50°$ in the xy-plane).

The measured spectra for two shots of different solenoid field strengths show a peak indicating focused electron energies in close agreement with the simulation predictions, as shown in Fig. 8(f). For the case $B_0 = 9.1$ T (blue), Boris pusher simulations predict a focused energy $E_f = 11.2$ MeV, which reproduces the measured focused energy. The measured spectrum is considerably broader than the predicted spectrum. Although we show that astigmatism at the level observed in Fig. 3 can account for some broadening of the spectrum [Fig. 8(f) dashed and solid blue lines, corresponding to the spatial profiles in Figs. 8(a) and 8(b), respectively], additional factors may contribute to the broader spectra we measure, such as repulsive space charge effects. For the simulated case

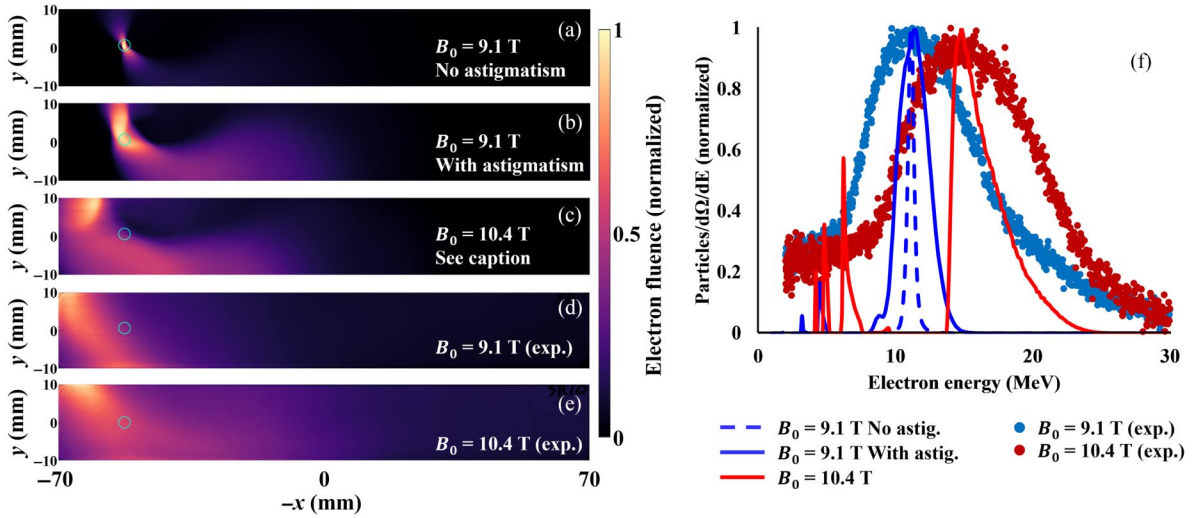


FIG 8. Boris pusher simulation predictions and experimental results of spatiospectral electron beam conditioning. For (a)–(e), electrons propagate into the page. (a), (b) Simulated electron beam spatial profiles without and with astigmatism, respectively. The input electron beam properties are given in Fig. 2(a) and 2(d), $(\theta_x, \theta_y) = (+5°, 0°)$, $B_0 = 9.1$ T, and $L_{\text{det}} = 343$ mm. In (b), the solenoid major and minor axes are 6.65 and 7.65 mm, respectively. (c) Simulated electron beam spatial profile with more severe astigmatism and with the electron beam pointing 45 mrad off of the optical axis. Here, the solenoid major and minor axes are 6.65 and 9.65 mm, respectively. (d), (e) Measured electron beam spatial profiles for $B_0 = 9.1$ and 10.4 T, respectively. The solenoid angle in the experiment was $(\theta_x, \theta_y) = (+5°, 0°) \pm (1°, 1°)$, and $L_{\text{det}} = 343$ mm. In (a)–(e), the OU-ESM 3-mm-diameter aperture, which is angled at +10° with respect to the optical axis, is superimposed in teal. Electrons propagating through the aperture contribute to (f) electron spectra corresponding to the three simulations described in (a)–(c) (curves) and the two experimental conditions described in (d), (e) (dots).

$B_0 = 10.4$ T, solenoid angle $(\theta_x, \theta_y) = (+6°, +1°)$, and electron beam pointing of 45 mrad (at an angle of +50° in the xy-plane), we find agreement in the predominantly focused energy (14.8 MeV) of the predicted spectrum and the measured spectrum.

V. CONCLUSION

Spatiospectral conditioning using electromagnetic solenoids is an elegant solution to some of the challenges faced by microcoulomb-class LPA electron beams at HEDS facilities. We have experimentally shown that this technique can focus electron beams to spot sizes down to 18 mm FWHM at our detector plane, and we measured an electron beam fluence enhancement factor of 6 over unconditioned electron beams. We measured electron radiography resolution improvement by up to a factor of 3 when using the conditioned electron beams compared to the unconditioned electron beams, demonstrating the benefits of solenoidal conditioning to a valuable electron beam application. Our measurements of electron beam spatial profiles and spectra resulting from on-axis and angled solenoidal focusing demonstrate proof of principle of the analytic theory and Boris pusher models, instilling confidence in these predictions for next-generation experiments.

This work found that the broader electron beam spatial profiles and spectra observed when conditioning electron beams with the solenoids compared to ideal simulations may be partially due to solenoid astigmatism and variations in the native electron beam spectrum. However, we found that electron beam focusability and electron beam radiography do not suffer tremendously due to the extent of solenoid astigmatism on our experimental platform. Follow-on studies may be conducted to assess the effects of space charge on the broadening of the experimental observables, especially the spectra. Finally, additional studies could investigate the effects of higher-order aberrations on the diamondlike beam profile, variations of which have also been observed in electron beams [47] and proton beams [57–59] focused by solenoids downstream of laser-based accelerators.

Future studies that aim to implement spatiospectral conditioning of LPA-produced electron beams will require precise manufacturing and alignment of the solenoids. Although the merits of spatiospectral conditioning were certainly demonstrated using these hand-wound solenoids, machine-wound solenoids with less solenoid-to-solenoid variation in the wire path should improve shot-to-shot reproducibility of the resulting electron beam conditioning. The astigmatism may be minimized by implementing machine-based coil winding techniques, but any astigmatism incurred in the coil due to its expansion as it is pulsed with current is likely unavoidable. Solenoid alignment is another critical parameter in these experiments. Deviations from ideal solenoid placement beyond 200 μm and

deviations from the desired solenoid angle beyond 2° will lead to the electron focus feature (Figs. 7 and 8) missing the target location at the detection plane. Full control of the solenoid position in 3D space and the solenoid angle in both xz- and yz-planes is crucial.

ACKNOWLEDGMENTS

The authors thank A. Raymond, K. R. McMillen, and S. McPoyle for useful discussions. The authors thank D. Canning and the OMEGA EP operational team for their support of the experiments. The authors thank T. Filkins, R. Rinefierd, and S. Hart for their contributions to the OU-ESM hardware modifications. This material is based upon the work supported by the U.S. Department of Energy, Office of Science, Office of Fusion Energy, under Award No. DE-SC0021057, and by the Department of Energy [National Nuclear Security Administration] University of Rochester "National Inertial Confinement Fusion Program" under Award No. DE-NA0004144. This report was prepared as an account of work sponsored by an agency of the United States Government. Neither the United States Government nor any agency thereof, nor any of their employees, makes any warranty, express or implied, or assumes any legal liability or responsibility for the accuracy, completeness, or usefulness of any information, apparatus, product, or process disclosed, or represents that its use would not infringe privately owned rights. Reference herein to any specific commercial product, process, or service by trade name, trademark, manufacturer, or otherwise does not necessarily constitute or imply its endorsement, recommendation, or favoring by the United States Government or any agency thereof. The views and opinions of authors expressed herein do not necessarily state or reflect those of the United States Government or any agency thereof.

M. V. A. led conceptualization, data curation, formal analysis, investigation, software development, validation, visualization, and the writing of the original draft, with an equal contribution to methodology. H. G. R. contributed equally to conceptualization and writing—review and editing, with supporting roles in formal analysis, methodology, supervision, and validation. J. P. provided supporting contributions to conceptualization, data curation, investigation, and methodology. D. F. provided supporting contributions to conceptualization, data curation, investigation, and methodology. R. M. provided supporting contributions to conceptualization, investigation, methodology, and software. C. D. A. contributed equally to conceptualization and provided supporting contributions to supervision and writing—review and editing. G. B. contributed equally to conceptualization, with supporting roles in data curation, formal analysis, investigation, methodology, software, validation, and writing—review and editing. I. A. L. and M. A. V.-G. provided supporting contributions to investigation. D. H. F. led funding acquisition and provided supporting contributions to conceptualization and supervision. J. L. S. contributed equally to conceptualization, led supervision and writing—review and editing, and provided supporting contributions to data curation, formal analysis, investigation, methodology, validation, and visualization.

The authors have no conflicts to disclose.

DATA AVAILABILITY

There are no publicly available research data or software supporting this manuscript. Requests for further information or data should be sent to the authors.

APPENDIX A: RELATIVISTIC BORIS PUSHER

The relativistic particle pusher used to calculate the electron trajectories in the simulations uses the Boris pusher algorithm [46] with relativistic corrections. Our solver neglects electric field contributions and space charge effects. The loop process is as follows:

(i) Begin by initializing each electron's position r and velocity v.

(ii) Define the first intermediate velocity $v^- \equiv \gamma v_{\text{prev}}$, where v_{prev} is the electron velocity at the previous time step and γ is the relativistic Lorentz factor.

(iii) Define the intermediate magnetic fields $t \equiv \frac{qB}{\gamma m}\frac{\Delta t}{2}$ and $s \equiv \frac{2t}{1+t^2}$, where q is the electron charge, B is the magnetic field strength, and m is the electron mass.

(iv) Rotate the intermediate velocity according to the magnetic field

(a) Solve for second intermediate velocity: $v' = v^- + v^- \times t$

(b) Solve for third intermediate velocity: $v^+ = v^- + v^- \times s$.

(v) Solve for the velocity at the next time step:

$$v_{\text{next}} = v^+ \frac{1}{\sqrt{1 + (v^+ \cdot v^+)/c^2}}. \tag{A1}$$

Update the particle position: $r_{\text{next}} = r_{\text{prev}} + v_{\text{next}}\Delta t$, where r_{prev} is the electron position at the previous time step and Δt is the time step of the simulation. The time step of the simulation was $\Delta t = 0.5$ ps, corresponding to 10 time steps per cyclotron period. A convergence test with 100 time steps per cyclotron period verified that $\Delta t = 0.5$ ps provided sufficient resolution. The energy binning used was 0.1 MeV in the range 1–30 and 1 MeV in the range 31–200 MeV.

Space charge effects become important to the dynamics of the electron beam when the so-called laminarity parameter, ρ, is very large [60]:

$$\rho = \frac{I\sigma^2}{2I_A\gamma\epsilon_n^2}, \tag{A2}$$

where I is the electron beam current, σ is the electron beam transverse rms beam size, $I_A \approx 17$ kA is the Alfvén current, and $\epsilon_n = \beta\gamma\epsilon$ is the normalized emittance with Lorentz factor γ and $\beta = v/c$. For nominal parameters of our electron beams in this study,

(i) $I = Q$ (total charge)/τ (electron beam pulse duration) = 500 nC/700 fs, (ii) $\sigma = 28$ μm, (iii) for an electron energy of 5.8 MeV (given by the measured peak electron energy of shot A in Fig. 3), $\beta = 0.9967$ and $\gamma = 12.35$, and (iv) $\epsilon_n = \beta\gamma\epsilon = \beta\gamma\sigma\theta = 0.9967 \times 12.35 \times 28\ [\mu\text{m}] \times 160\ [\text{mrad}] = 5.57 \times 10^{-5}\ [\text{m} \cdot \text{rad}]$, where θ is the full-angle divergence of the electron beam as it exits the gas jet.

This yields $\rho \approx 0.44$. Therefore, the dynamics of the electron beams in our experiment are not dominated by space charge effects. Space charge effects are reduced further by the solenoid due to the chromatic nature of solenoidal focusing. Since electrons of different energies have different focal lengths and because our electron beam spectrum has a broad distribution, the electron beam is more spread out in the space between the solenoid and the detector as the different energies come in and out of focus. This longitudinal chromatism is especially true for lower-energy electrons where space charge forces would dominate in the absence of solenoid focusing owing to the strong scaling with γ in the laminarity parameter.

APPENDIX B: ELECTRON ENERGY-DEPENDENT FOCAL LENGTH OF A SOLENOID

The imaging properties of a solenoid can be derived from the electron equation of motion as it propagates through the solenoid. A full derivation is given in [52], and key results and their implications are in italics below.

1. For a cylindrically symmetric solenoid, the radial displacement of an electron, r, with respect to an axis co-located with the solenoid axis, z, is given by

$$\frac{d^2r}{dz^2} = -\frac{e^2c^2}{4(E_k^2 + 2E_kE_0)} B_z^2(z)\, r(z) = -G(z)r(z), \tag{B1}$$

where e is the electron charge, c is the vacuum speed of light, E_k is the electron kinetic energy, E_0 is the electron rest energy, and $B_z(z)$ is the longitudinal component of the magnetic field.

2. To arrive at an equation of a solenoid focal length with potentially multiple foci for lower-energy electrons, assume the solenoid magnetic field follows Glaser's bell-shaped field [48],

$$B(z) = \frac{B_0}{1 + (z/a)^2}, \tag{B2}$$

where B_0 is the magnetic field at the solenoid center and a is the full width half maximum of $B(z)$ (in practice, this is approximately the solenoid radius).

Using reduced coordinates $y = r/a$ and $x = z/a$ and defining

$$k^2 = \frac{e^2c^2B_0^2a^2}{4(E_k^2 + 2E_kE_0)}, \tag{B3}$$

we can rewrite (B1) as

$$\frac{d^2y}{dx^2} = -\frac{k^2}{(1+x^2)^2}\, y(x). \tag{B4}$$

3. For obviously oscillatory solutions, apply the substitution, $x = \cot\phi, 0 \le \phi \le \pi$, such that $dx = -d\phi/\sin^2\phi$ and $1 + x^2 = \csc^2\phi$. The geometrical interpretation of ϕ is as follows: For electrons approaching the solenoid from infinitely far away ($z \to -\infty$), $\phi = \pi$. At the center of the solenoid ($z = 0$), $\phi = \pi/2$. For electrons leaving the solenoid infinitely far away ($z \to +\infty$), $\phi = 0$. The final electron equation of motion is

$$\frac{d^2y}{d\phi^2} + 2\cot\phi\frac{dy}{d\phi} + k^2\, y(\phi) = 0, \tag{B5}$$

which has solutions of the form

$$y(\phi) = C_1\frac{\sin(\omega\phi)}{\sin(\phi)} + C_2\frac{\cos(\omega\phi)}{\sin(\phi)}, \tag{B6}$$

where C_1 and C_2 are coefficients determined by the electron's initial position and momentum and

$$\omega = \sqrt{1 + k^2} \tag{B7}$$

is a lens strength parameter.

4. For an electron passing through an initial point $P_0(y_0, \phi_0)$, $C_1 = \frac{y_0\sin\phi_0}{\sin(\omega\phi_0)} - \frac{C_2\cos(\omega\phi_0)}{\sin(\omega\phi_0)}$. Plugging this result back into (B6) yields

$$y(\phi) = \frac{\sin(\omega\phi)\sin\phi_0}{\sin(\omega\phi_0)\sin\phi}y_0 + \frac{C_2}{\sin\phi}\left[\cos(\omega\phi) - \frac{\cos(\omega\phi_0)}{\sin(\omega\phi_0)}\sin(\omega\phi)\right]. \tag{B8}$$

5. The image point $P_1(y_1, \phi_1)$ conjugate to the object point P_0 can be obtained by setting the bracket to zero.

The bracket portion is zero when $\sin[\omega(\phi_1 - \phi_0)] = 0$, which is satisfied by

$$\phi_{1n} = \phi_0 - \frac{n\pi}{\omega}, \quad \text{for } n = 1, 2, \ldots \tag{B9}$$

Thus, multiple image points (for multiple electron energies) can occur once $\omega \geq 2$ (i.e., for sufficiently strong solenoid field strengths).

Incidentally, (B8) also provides the divergence-independent magnification, M,

$$y_1 = \frac{\sin(\omega\phi_1)\sin\phi_0}{\sin(\omega\phi_0)\sin\phi_1} y_0 = M\, y_0. \tag{B10}$$

6. To arrive at a focal length of the solenoid, consider the object point $z_0 = a\cot\phi_0$ and image points $z_{1n} = a\cot\phi_{1n}$. Substituting (B9) into the definition for the object point and rearranging yields

$$\left[z_0 - a\cot\left(\frac{n\pi}{\omega}\right)\right]\left[z_{1n} + a\cot\left(\frac{n\pi}{\omega}\right)\right] = -a^2\csc^2\left(\frac{n\pi}{\omega}\right). \tag{B11}$$

This is equivalent to Newton's lens equation of light optics: $Z_0 Z_1 = f_0 f_1$, where $Z_0 = z_0 - z(F_0)$ and $Z_1 = z_1 - z(F_1)$ separate the object and image points from the corresponding foci.

The focal lengths of the solenoid are given by

$$f_0 = -f_1 = a\csc\left(\frac{n\pi}{\omega}\right) \tag{B12}$$

and the distances of the foci from the lens center at $z = 0$ are given by

$$z(F_0) = -z(F_1) = a\cot\left(\frac{n\pi}{\omega}\right). \tag{B13}$$

The results of (B12) and (B13) show that the focal lengths are *not* equal to the distances of the foci from the lens center—this implies that rigorously, *solenoids cannot be treated as thin lenses*, and principal planes must be introduced for where the electron refraction takes place. *However, for the solenoids and electron beams used in this study, we have found agreement to within* ± 0.5 MeV *in the focused electron energy as calculated from the thin-lens approximation, the bell-shaped-field approximation, Boris pusher simulations, and as measured in experiments*.

7. Solving (B11) for ω ultimately yields the electron energies focused at the image plane,

$$E_f = \frac{-4K^2(n)E_0 + \sqrt{(2K^2(n)E_0)^2 + 4K^2(n)e^2c^2B_0^2a^2}}{4K^2(n)}, \tag{B14}$$

where

$$K^2(n) \equiv \Omega^2(n) - 1 \tag{B15}$$

and

$$\Omega(n) = \frac{n\pi}{\pi - \cot^{-1}\left(\frac{a^2 + z_0 z_1}{a z_0 - a z_1}\right)}. \tag{B16}$$

To use (B14)–(B16) to predict the observed focused electron energies, set z_0 as the distance between the electron source location and the solenoid and set z_1 as the distance between the solenoid and the detection plane. The sign convention is $z_0 < 0$ and $z_1 > 0$. The predominant focus feature occurs for $n = 1$.

[1] B. K. Russell, P. T. Campbell, Q. Qian, J. A. Cardarelli, S. S. Bulanov, S. V. Bulanov, G. M. Grittani, D. Seipt, L. Willingale, and A. G. R. Thomas, Ultrafast relativistic electron probing of extreme magnetic fields, Phys. Plasmas **30**, 093105 (2023).

[2] C. J. Zhang *et al.*, Capturing relativistic wakefield structures in plasmas using ultrashort high-energy electrons as a probe, Sci. Rep. **6**, 29485 (2016).

[3] G. Bruhaug, M. S. Freeman, H. G. Rinderknecht, L. P. Neukirch, C. H. Wilde, F. E. Merrill, J. R. Rygg, M. S. Wei, G. W. Collins, and J. L. Shaw, Single-shot electron radiography using a laser–plasma accelerator, Sci. Rep. **13**, 2227 (2023).

[4] C. Xiao *et al.*, Design of a compact electron radiography system with electron source from laser wakefield accelerator, AIP Adv. **11**, 045030 (2021).

[5] M. J. V. Streeter *et al.*, Narrow bandwidth, low-emittance positron beams from a laser-wakefield accelerator, Sci. Rep. **14**, 6001 (2024).

[6] Y. Noh *et al.*, Charge-neutral, GeV-scale electron-positron pair beams produced using bremsstrahlung gamma rays, Commun. Phys. **7**, 44 (2024).

[7] H.-I. Kim, Y. Noh, J. Song, S. Lee, J. Won, C. Song, L. Bae, C.-M. Ryu, C. H. Nam, and W. Bang, Electron-positron generation by irradiating various metallic materials with laser-accelerated electrons, Results Phys. **57**, 107310 (2024).

[8] G. Sarri *et al.*, Laser-driven generation of collimated ultra-relativistic positron beams, Plasma Phys. Control. Fusion **55**, 124017 (2013).

[9] I. M. Pagano, N. Lemos, P. M. King, D. Rusby, M. Sinclair, A. Aghedo, S. Khan, M. C. Downer, C. Joshi, and F. Albert, Source size of x rays from self-modulated laser wakefield accelerators, Phys. Plasmas **31**, 073110 (2024).

[10] F. Albert, Principles and applications of x-ray light sources driven by laser wakefield acceleration, Phys. Plasmas **30**, 050902 (2023).

[11] N. Lemos, J. L. Martins, F. S. Tsung, J. L. Shaw, K. A. Marsh, F. Albert, B. B. Pollock, and C. Joshi,

Self-modulated laser wakefield accelerators as x-ray sources, Plasma Phys. Control. Fusion **58**, 034018 (2016).
[12] N. Lemos *et al.*, X-ray sources using a picosecond laser driven plasma accelerator, Phys. Plasmas **26**, 083110 (2019).
[13] P. M. King *et al.*, X-ray analysis methods for sources from self-modulated laser wakefield acceleration driven by picosecond lasers, Rev. Sci. Instrum. **90**, 033503 (2019).
[14] F. Albert *et al.*, Betatron x-ray radiation from laser-plasma accelerators driven by femtosecond and picosecond laser systems, Phys. Plasmas **25**, 056706 (2018).
[15] N. Lemos *et al.*, Bremsstrahlung hard x-ray source driven by an electron beam from a self-modulated laser wakefield accelerator, Plasma Phys. Control. Fusion **60**, 054008 (2018).
[16] F. Albert *et al.*, Observation of betatron X-ray radiation in a self-modulated laser wakefield accelerator driven with picosecond laser pulses, Phys. Rev. Lett. **118**, 134801 (2017).
[17] C. McGuffey *et al.*, On the properties of synchrotron-like X-ray emission from laser wakefield accelerated electron beams, Phys. Plasmas **25**, 043104 (2018).
[18] M. Kozlova *et al.*, Hard X rays from laser-wakefield accelerators in density tailored plasmas, Phys. Rev. X **10**, 011061 (2020).
[19] S. Kneip *et al.*, Observation of synchrotron radiation from electrons accelerated in a petawatt-laser-generated plasma cavity, Phys. Rev. Lett. **100**, 105006 (2008).
[20] A. Rousse *et al.*, Production of a keV X-ray beam from synchrotron radiation in relativistic laser-plasma interaction, Phys. Rev. Lett. **93**, 13 (2004).
[21] E. Esarey, B. A. Shadwick, P. Catravas, and W. P. Leemans, Synchrotron radiation from electron beams in plasma-focusing channels, Phys. Rev. E **65**, 15 (2002).
[22] H. P. Schlenvoigt *et al.*, A compact synchrotron radiation source driven by a laser-plasma wakefield accelerator, Nat. Phys. **4**, 130 (2008).
[23] A. Döpp, L. Hehn, J. Götzfried, J. Wenz, M. Gilljohann, H. Ding, S. Schindler, F. Pfeiffer, and S. Karsch, Quick x-ray microtomography using a laser-driven betatron source, Optica **5**, 199 (2018).
[24] S. Fourmaux *et al.*, Single shot phase contrast imaging using laser-produced betatron x-ray beams, Opt. Lett. **36**, 2426 (2011).
[25] J. M. Cole *et al.*, Tomography of human trabecular bone with a laser-wakefield driven x-ray source, Plasma Phys. Control. Fusion **58**, 014008 (2015).
[26] J. Feng, Y. Li, J. Wang, D. Li, F. Li, W. Yan, W. Wang, and L. Chen, Gamma-ray emission from wakefield-accelerated electrons wiggling in a laser field, Sci. Rep. **9**, 2531 (2019).
[27] X. J. Jiao *et al.*, A tabletop, ultrashort pulse photoneutron source driven by electrons from laser wakefield acceleration, Matter Radiat. Extremes **2**, 296 (2017).
[28] J. Feng *et al.*, High-efficiency neutron source generation from photonuclear reactions driven by laser plasma accelerator, High Energy Density Phys. **36**, 100753 (2020).
[29] Y. Li, J. Feng, W. Wang, J. Tan, X. Ge, F. Liu, W. Yan, G. Zhang, C. Fu, and L. Chen, Micro-size picosecond-duration fast neutron source driven by a laser-plasma wakefield electron accelerator, High Power Laser Sci. Eng. **10**, 33 (2022).
[30] S. Vallières *et al.*, High average-flux laser-driven neutron source, Nat. Commun. **16**, 11498 (2025).
[31] J. L. Shaw *et al.*, Microcoulomb ($0.7 \pm 0.40.2$ μC) laser plasma accelerator on OMEGA EP, Sci. Rep. **11**, 7498 (2021).
[32] F. Albert *et al.*, Microcoulomb electron beams from self-modulated laser wakefield acceleration at the National Ignition Facility, in *62nd Annual Meeting of the APS Division of Plasma Physics* (American Institute of Physics (AIP) Publishing, Melville, NY, 2020).
[33] W. Cayzac *et al.*, Experimental capabilities of the LMJ-PETAL facility, High Energy Density Phys. **52**, 101125 (2024).
[34] R. L. Taylor, Magnetic measurements of quadrupole focusing magnets at SLAC, Am. J. Phys. (1991).
[35] D. J. Harding *et al.*, A wide aperture quadrupole for the fermilab main injector synchrotron, in *22nd Particle Accelerator Conference* (Institute of Electrical and Electronics Engineers (IEEE), Piscataway, NJ, 2007).
[36] R. Dowd, M. Boland, G. LeBlanc, and Y.-R. E. Tan, Achievement of ultralow emittance coupling in the Australian synchrotron storage ring, Phys. Rev. ST Accel. Beams **14**, 012804 (2011).
[37] R. Weingartner *et al.*, Imaging laser-wakefield-accelerated electrons using miniature magnetic quadrupole lenses, Phys. Rev. ST Accel. Beams **14**, 386 (2011).
[38] J. Rosenzweig, Products—RadiaBeam, https://radiabeam.com/products/products/.
[39] H. Busch, Berechnung der Bahn von Kathodenstrahlen in axial symmetrischen electromagnetischen Felde, Zeitschrift Für Physik **81**, 25 (1926).
[40] P. Hawkes and E. Kasper, *Principles of Electron Optics, Volume 1: Basic Geometrical Optics*, 2nd ed. (Academic Press, Cambridge, MA, 2017), Vol. 1.
[41] D. D. Meyerhofer *et al.*, *Performance of and Initial Results from the OMEGA EP Laser System*, Journal of Physics: Conference Series (Institute of Physics Publishing, Bristol, UK, 2010), Vol. 244.
[42] C. Dorrer, A. Consentino, D. Irwin, J. Qiao, and J. D. Zuegel, OPCPA front end and contrast optimization for the OMEGA EP kilojoule, picosecond laser, J. Optics (United Kingdom) **17**, 094007 (2015).
[43] K. R. McMillen, P. V. Heuer, J. M. Gjevre, A. L. Milder, P. Charles, T. Filkins, H. G. Rinderknecht, D. H. Froula, and J. L. Shaw, Validation of predictive performance models for supersonic gas-jet nozzles at the laboratory for laser energetics, Rev. Sci. Instrum. **95**, 073517 (2024).
[44] R. V. Shapovalov, G. Brent, R. Moshier, M. Shoup, R. B. Spielman, and P.-A. Gourdain, Design of 30-T pulsed magnetic field generator for magnetized high-energy-density plasma experiments, Phys. Rev. Accel. Beams **22**, 080401 (2019).
[45] H. Chen, G. Fiksel, D. Barnak, P.-Y. Chang, R. F. Heeter, A. Link, and D. D. Meyerhofer, Magnetic collimation of relativistic positrons and electrons from high intensity laser-matter interactions, Phys. Plasmas **21**, 040703 (2014).
[46] J. P. Boris, Relativistic plasma simulation - optimization of a hybrid code, in *Proceeding of 4th Conference on*

Numerical Simulation of Plasmas, edited by J. P. Boris and R. A. Shanny (U. S. Government Printing Office, Washington, D. C., 1971), pp. 3–67.

[47] Y. Sakai *et al.*, Narrow band and energy selectable plasma cathode for multistage laser wakefield acceleration, Phys. Rev. Accel. Beams **21**, 101301 (2018).

[48] W. Glaser, *Grundlagen Der Elektronenoptik* (Springer, Vienna, Austria, 1952).

[49] H. Chen, A. J. Link, R. Van Maren, P. K. Patel, R. Shepherd, S. C. Wilks, and P. Beiersdorfer, High performance compact magnetic spectrometers for energetic ion and electron measurement in ultraintense short pulse laser solid interactions in review of scientific instruments, Rev. Sci. Instrum. **79**, 10E533 (2008).

[50] J. L. Shaw, Self-modulated laser wakefield acceleration for OMEGA EP, in *61st Annual Meeting of the APS Division of Plasma Physics* (American Institute of Physics (AIP) Publishing, Melville, NY, 2019).

[51] S. Leisegang, Zum astigmatismus von elektronenlinsen, Optik (Stuttg). **10**, 5 (1953).

[52] L. Reimer, *Transmission Electron Microscopy : Physics of Image Formation and Microanalysis* (Springer, New York, New York, 1997).

[53] R. F. Egerton, *Physical Principles of Electron Microscopy* (Springer, New York, New York, 2005).

[54] A. Nassiri, Stopping power and scattering angle calculations of charged particle beams through thin foils (1991).

[55] B. Blind and A. J. Jason, Chromatically corrected imaging systems for charged-particle radiography, in *21st Particle Accelerator Conference* (Institute of Electrical and Electronics Engineers (IEEE), Piscataway, NJ, 2005).

[56] H. Habara, T. Iwawaki, T. Gong, M. S. Wei, S. T. Ivancic, W. Theobald, C. M. Krauland, S. Zhang, G. Fiksel, and K. A. Tanaka, A ten-inch manipulator (TIM) based fast-electron spectrometer with multiple viewing angles (OU-ESM), Rev. Sci. Instrum. **90**, 063501 (2019).

[57] K. Harres *et al.*, *Beam Collimation and Transport of Laser-Accelerated Protons by a Solenoid Field*, Journal of Physics: Conference Series (IOP Publishing, Bristol, UK, 2010), Vol. 244, p. 022036.

[58] T. Burris-Mog *et al.*, Laser accelerated protons captured and transported by a pulse power solenoid, Phys. Rev. ST Accel. Beams **14**, 121301 (2011).

[59] M. Tayyab, S. Bagchi, R. Husain, S. Bidoliya, M. L. Sharma, K. Aneesh, S. Nigam, A. Moorti, and J. A. Chakera, Laser-plasma accelerated proton beam transport system using high-field pulsed solenoid magnet, Nucl. Instrum. Methods Phys. Res. A **1065**, 169488 (2024).

[60] M. Ferrario, M. Migliorati, and L. Palumbo, Space charge effects, in *Proceedings of the CAS-CERN Accelerator School: Advanced Accelerator Physics*, edited by W. Herr (CERN, Trondheim, Norway, 2013).